Research article

Yue Yu, Lai Wang and Xiankai Sun*

Demonstration of on-chip gigahertz acousto-optic modulation at near-visible wavelengths

https://doi.org/10.1515/nanoph-2021-0330
Received June 30, 2021; accepted August 26, 2021;
published online September 24, 2021

Abstract: Lithium niobate integrated photonics has recently received significant attention because it exploits the attractive properties of lithium niobate on an integrated platform which provides strong optical confinement as well as high photonic integration density. Although many optical functionalities of lithium niobate have been demonstrated on a chip in the telecom band, the visible and near-visible regimes are less explored. This is mainly because devices with a relatively smaller feature size are required which increases fabrication difficulty. Here, we explored the acousto-optic effect of lithium niobate on a chip at near-visible wavelengths (765–781 nm) and demonstrated acousto-optic modulation with the modulation frequency up to 2.44 GHz. We adopted an etchless process for the device fabrication and applied the principle of bound states in the continuum to optimize the device performance. By demonstrating functionality at near-visible wavelengths, our devices will enable many on-chip applications ranging from frequency metrology to quantum information processing.

Keywords: acousto-optic modulation; bound states in the continuum; visible photonics.

1 Introduction

Visible integrated photonics, albeit less prevalent than the well-developed telecom integrated photonics, has distinctive applications, such as biosensing [1–3], quantum information processing [4–7], and frequency metrology [8, 9]. Considering that half of the telecom wavelengths is within the visible range, visible integrated photonics is an indispensable component for realizing nonlinear integrated photonics. Various materials such as Si_3N_4 [10–13], SiO_2 [14, 15], AlN [16], Ta_2O_5 [17], and lithium niobate [18] have been adopted for visible integrated photonics. Among these materials, lithium niobate is the most promising candidate for visible integrated photonic platform due to its wide transparency window (400–5000 nm) [19], large piezoelectric, electro-optic, and nonlinear coefficients, which enable many nonlinear applications in frequency metrology and quantum information processing in a wide wavelength range. In conventional photonic integrated circuits, a smaller feature size is required for shorter working wavelength, which adds to fabrication difficulty. Additionally, the conventional method of fabricating photonic integrated circuits involves etching of the optical functional material, which introduces scattering loss at the etched edges. These challenges have recently been solved by adopting a fundamentally new photonic architecture and applying the principle of "bound states in the continuum (BICs)" [20–24]. Such photonic architectures can be fabricated by depositing and then lithographically patterning a fabrication-friendly material on the substrate without the need for etching the substrate material. This strategy has enabled many passive and active integrated photonic devices [25–28].

Acousto-optics, which deals with changes of refractive index of a medium in the presence of sound waves in the same medium, has aroused great interest due to its wide applications in deflection, modulation, signal processing, and frequency shifting of light beams. To achieve strong acousto-optic interaction, two conditions need to be satisfied: high energy confinement of optical and acoustic modes and large overlap between the two modes. Compared with bulk acoustic waves, surface acoustic waves (SAWs), which propagate on surfaces of a material with amplitude decaying exponentially within a depth less than acoustic wavelength, has very high energy confinement and can attain large overlap with the optical mode of a planar waveguide on an integrated

***Corresponding author: Xiankai Sun**, Department of Electronic Engineering, The Chinese University of Hong Kong, Shatin, New Territories, Hong Kong, E-mail: xksun@cuhk.edu.hk. https://orcid.org/0000-0002-9137-0298
Yue Yu, Department of Electronic Engineering, The Chinese University of Hong Kong, Shatin, New Territories, Hong Kong. https://orcid.org/0000-0002-6982-3115
Lai Wang, Department of Electronic Engineering, Beijing National Research Center for Information Science and Technology (BNRist), Tsinghua University, Beijing 100084, China

platform [29]. SAWs have recently been explored for a wide range of applications including frequency shifting [30, 31], nonreciprocal transmission [32], microwave-to-optical conversion [33], and microwave signal filtering [34]. Therefore, harnessing SAWs for visible integrated photonics can produce applications in visible-light optical signal processing, modulation, and filtering, which will pave the way for on-chip optical communication in the visible regime.

2 Results

We experimentally demonstrated gigahertz acousto-optic modulation on an integrated lithium niobate platform at near-visible wavelengths (765–781 nm). We patterned a racetrack microcavity in a polymer (ZEP520A) on a lithium-niobate-on-insulator substrate. The geometry of the cavity waveguide was engineered such that it could support propagating BICs inside the microcavity [26]. We fabricated two identical SAW interdigital transducers (IDTs) which were located symmetrically on the two sides of the waveguide in a straight section of the racetrack microcavity. One IDT was used for electrically exciting a propagating SAW, with frequency Ω, in the lithium niobate layer. The other IDT was electrically short and thus served as a reflector for the excited propagating SAW. These two IDTs produced an interference pattern for the SAWs. Since lithium niobate was not etched during device fabrication, those SAWs could propagate smoothly in the lithium niobate layer with negligible scattering loss and modulate the effective refractive index of the optical modes at frequency ω in the cavity waveguide. We have measured acousto-optic modulation of the racetrack microcavity with the modulation frequency up to 2.44 GHz, which was limited by the bandwidth of the visible photodetector (3.5 GHz).

Figure 1a illustrates the device for acousto-optic modulation of a racetrack microcavity on a lithium-niobate-on-insulator substrate. Figure 1b shows the cross section of the SAW-modulation region, where the yellow parts denote the SAW IDTs made of gold, the dark blue part denotes the polymer waveguide made of ZEP520A, the light blue part denotes the lithium niobate layer, and the gray part denotes the silicon oxide (the insulator). The thicknesses of the polymer waveguide, the lithium niobate layer, and the underlying silicon oxide layer are 400 nm, 150 nm, and 2 μm, respectively. Figure 1c plots the effective refractive index distributions for the waveguide structure shown in Figure 1b. Since the effective refractive index for the transverse electric (TE) polarization is higher than that for the transverse magnetic (TM) polarization, the TM-polarized bound mode lies in the TE-polarized continuous spectrum. This means that the TM bound mode can interact with the TE continuous modes, yielding energy dissipation of the former. The electric field ($|\mathbf{E}|$) distributions of a typical TM bound mode and TE continuous mode are provided in Figure 1c as insets. By engineering the width of the waveguide, the loss of the TM bound mode to the TE continuum can be eliminated by designing perfect destructive interference between different dissipation channels. This leads to a TM bound mode with zero theoretical propagation loss, which is referred to as the bound state in the continuum [21]. To acquire a high-quality racetrack microcavity, one should minimize the loss in both the straight and bent waveguides of the cavity simultaneously. In our previous work, we showed that the radiation loss of a bent waveguide depends on both the bend radius R and the waveguide width w [21]. For simplicity, the bend radius R was set as large as possible to facilitate engineering of the total loss of the racetrack microcavity, and thus $R = 150$ μm was adopted in our device. Figure 1d shows the calculated propagation loss of both the straight and bent waveguides as a function of waveguide width w.

Figure 2a and b are optical microscope images of the fabricated device with and without IDTs, respectively. Figure 2c is a close-up view of the acousto-optic modulation region. We chose the width of all the waveguides as $w = 1.5$ μm to minimize the intrinsic loss of the microcavity. The aperture of the IDTs is equal to the length of the straight section of the racetrack microcavity (i.e., $L = 140$ μm). To obtain maximal acousto-optic modulation, the IDTs are oriented along the x axis considering the anisotropic photoelastic coefficients of lithium niobate [35]. The period p of the IDTs is equal to the SAW wavelength λ_{SAW} as $p = \lambda_{SAW} = v_{SAW}/f_{SAW}$, where v_{SAW} and f_{SAW} are the velocity and frequency of the excited SAW, respectively. The period is set as $p = 2w = 3$ μm. The width of the IDT fingers is $p/4 = 0.75$ μm. The number of periods for both the IDTs is 40. Based on these design parameters, the acousto-optic modulation operates in the Bragg regime [36], where only one diffracted wave is produced essentially. The SAWs excited by the left IDT are reflected upon arriving at the right IDT. The excited and reflected acoustic waves interfere with each other, producing a standing wave whose amplitude profile does not vary in time. The amplitude of a standing wave at the antinode is twice that of the excited

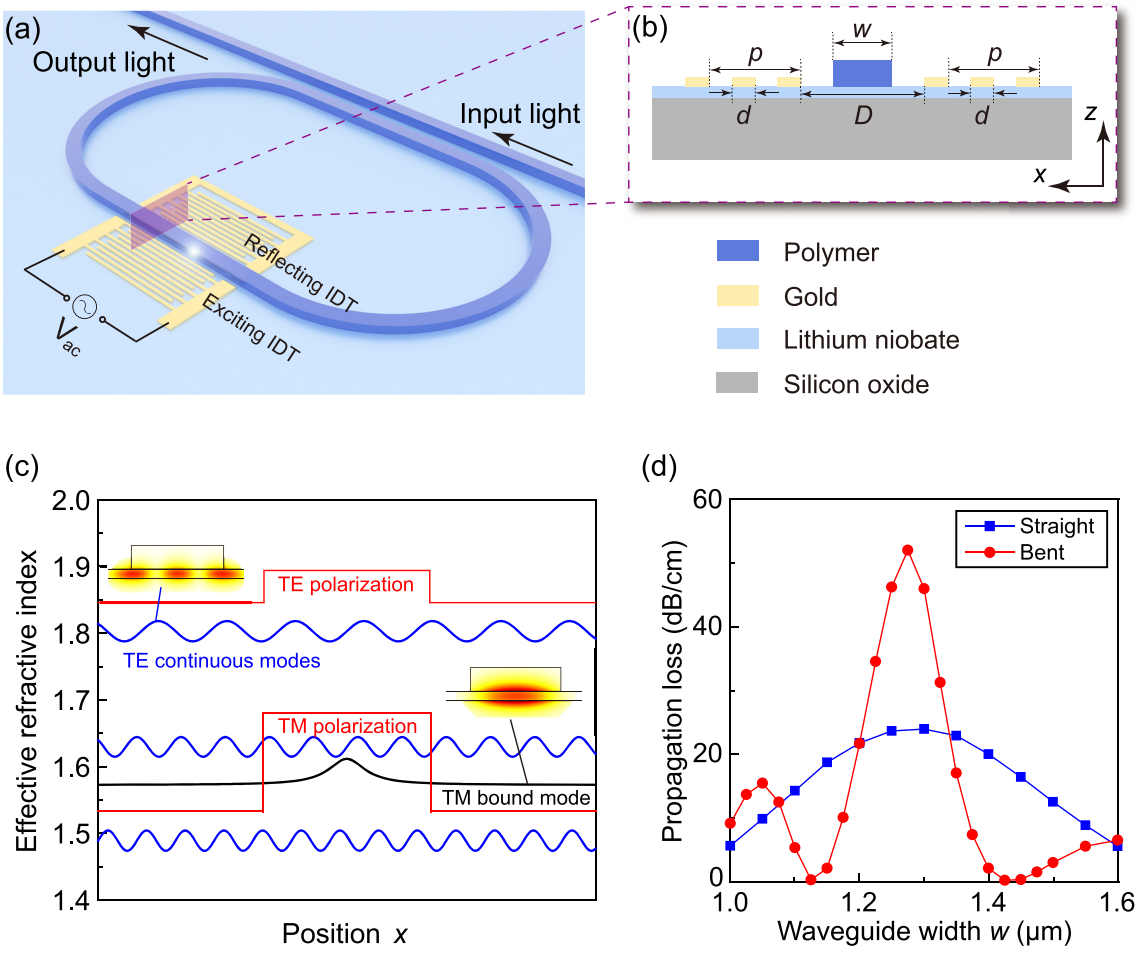

Figure 1: (a) Illustration of the device for acousto-optic modulation. (b) Cross section of the acousto-optic modulation region, with dimension labels. *w* is the width of the polymer waveguide, *p* is the period of the IDTs, *d* is the width of the IDT fingers, and *D* is the distance between the two IDTs. (c) Effective refractive index distributions for the TE- and TM-polarized modes in the waveguide structure in (b). The insets show the electric field |**E**| profiles of the TE continuous mode and the TM bound mode. (d) Calculated propagation loss of a straight waveguide and a bent waveguide with the bend radius of 150 μm.

wave. Therefore, the waveguide in the acousto-optic modulation region should be placed at an amplitude maximum of the SAWs. The distance D between the two IDTs should satisfy $D = 2m\lambda_{SAW} = 2mp$ (m is an integer), which was chosen to be 6 μm in this work.

A high-Q microcavity is prerequisite to achieving strong acousto-optic modulation. Figure 2d shows the measured optical transmission spectrum of the designed racetrack microcavity without IDTs (Figure 2a). Light from a tunable semiconductor laser (New Focus Velocity TLB-6712) was coupled into and out of the device under test via grating couplers to measure the transmission at different wavelengths. In the zoomed-in spectrum, the Lorentzian fit of a resonance near 773 nm indicates a loaded and an intrinsic optical Q factor of 1.4×10^5 and 3.1×10^5 respectively, which are comparable with those of etched lithium niobate microring resonators [18]. Figure 2e shows the measured optical transmission spectrum of the same racetrack microcavity with IDTs (Figure 2b). In the zoomed-in spectrum, the Lorentzian fit of a resonance near 773 nm indicates an intrinsic optical Q factor of 4.0×10^4. The reason for reduction in optical Q factor after adding the IDTs is considered to be caused by geometric deviation of the waveguide section that is sandwiched by the IDTs, because of the extra electron beam scattering by the adjacent electrodes during the electron-beam lithography for patterning the waveguides in the polymer layer.

Figure 3a shows the experimental setup for measuring the acousto-optic modulation. Light from a tunable

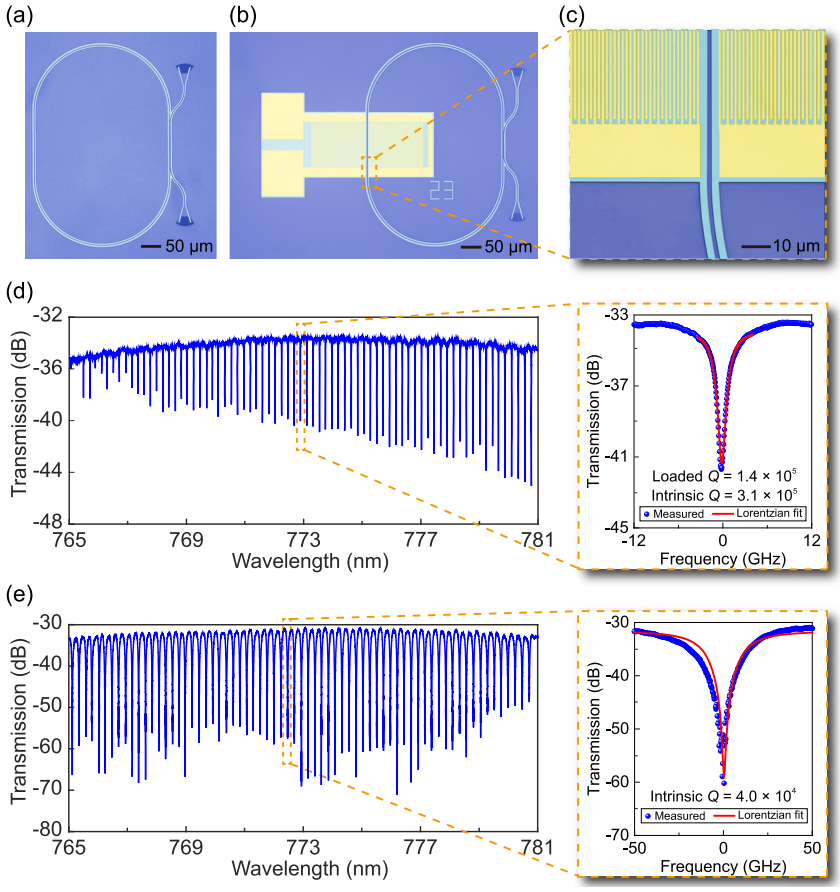

Figure 2: (a, b) Optical microscope image of the fabricated device without (a) and with (b) IDTs. (c) Close-up view of the acousto-optic modulation region. (d, e) Measured optical transmission spectrum (left) and zoomed-in spectrum near 773 nm (right) of the racetrack microcavity without (d) and with (e) IDTs. The blue dots represent the measured data and the red line is the corresponding Lorentzian fit.

semiconductor laser was sent through a fiber polarization controller (FPC) before being coupled into the device under test, where the FPC was used to select the desired TM polarization for optimal coupling. Meanwhile, a vector network analyzer (Keysight E5071C) delivered from its Port 1 a sinusoidal microwave signal to the SAW IDT via a microwave probe. The wavelength of the laser was slightly detuned from an optical resonance. The acousto-optically modulated light was enhanced by the optical resonance. With an output grating coupler, the acousto-optically modulated light was coupled out of the device chip. 1% of the output light was sent to a high-sensitivity photodetector PD1 (HP 81530A) for monitoring the optical transmission, while 99% was collected by a high-speed photodetector PD2 (New Focus 1591NF) and then sent back to Port 2 of the vector network analyzer. Figure 3b plots the recorded S_{11} spectrum under a delivered microwave signal power of −5 dBm, where several excited SAW modes are identified as the dips labeled as ①–⑥ with the highest frequency being 2.44 GHz. We used COMSOL to simulate the SAWs in our device where the period of the IDTs is 3 μm. Figure 3c presents the cross-sectional displacement fields for the SAW modes labeled in Figure 3b, which shows excellent agreement between the simulated and experimental results. Figure 4a plots the measured S_{21} spectrum of our fabricated device, which shows the frequency response of acousto-optic modulation. All the labeled dips in the S_{11} spectrum in Figure 3b can also be found in the S_{21} spectrum in Figure 4a. Figure 4b–g plot the individual zoomed-in spectra with their Lorentzian fits for the SAW modes labeled in Figure 4a.

3 Discussion and conclusion

In conclusion, we have demonstrated on-chip gigahertz acousto-optic modulation at near-visible wavelengths on a lithium-niobate-on-insulator platform. By designing the waveguide structure under the BIC principle, we could pattern a low-refractive-index, fabrication-friendly polymer for realizing low-loss waveguides and high-Q cavities on an integrated lithium niobate platform without the need for etching lithium niobate, thus significantly simplifying the fabrication processes. We used two IDTs, one for exciting and the other for reflecting the SAWs, on the two sides of a straight section of the racetrack microcavity for

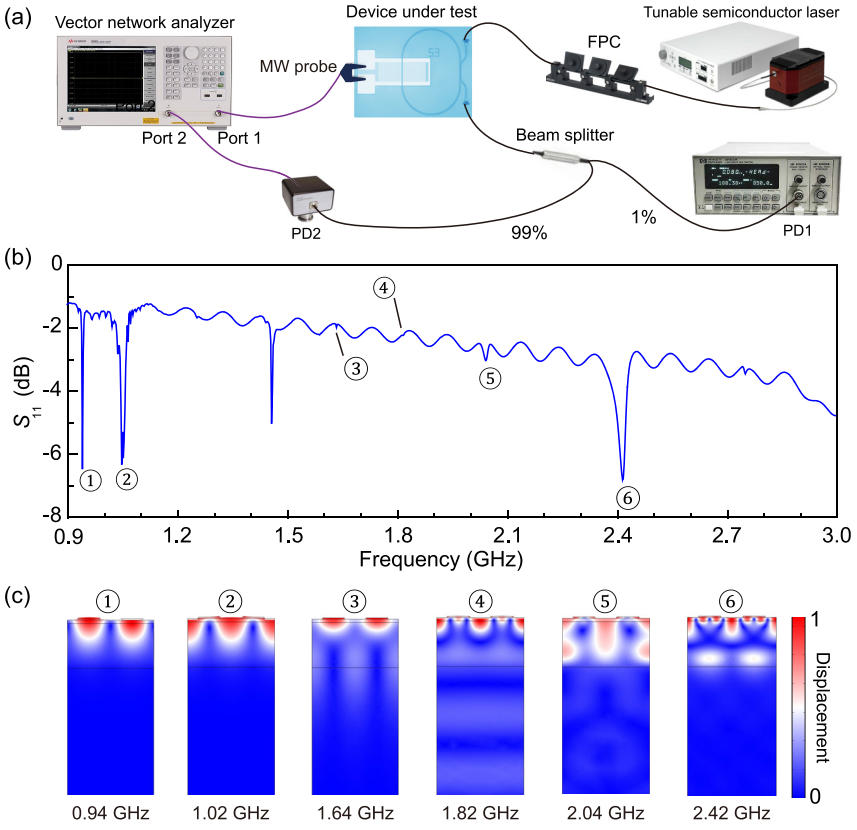

Figure 3: (a) Experimental setup for measuring the acousto-optic modulation. MW probe, microwave probe; FPC, fiber polarization controller; PD1, high-sensitivity photodetector; PD2, high-speed photodetector. (b) Measured S_{11} spectrum, where the excited SAW modes are identified as the dips labeled as ①–⑥. (c) Cross-sectional displacement profiles for the SAW modes labeled in (b).

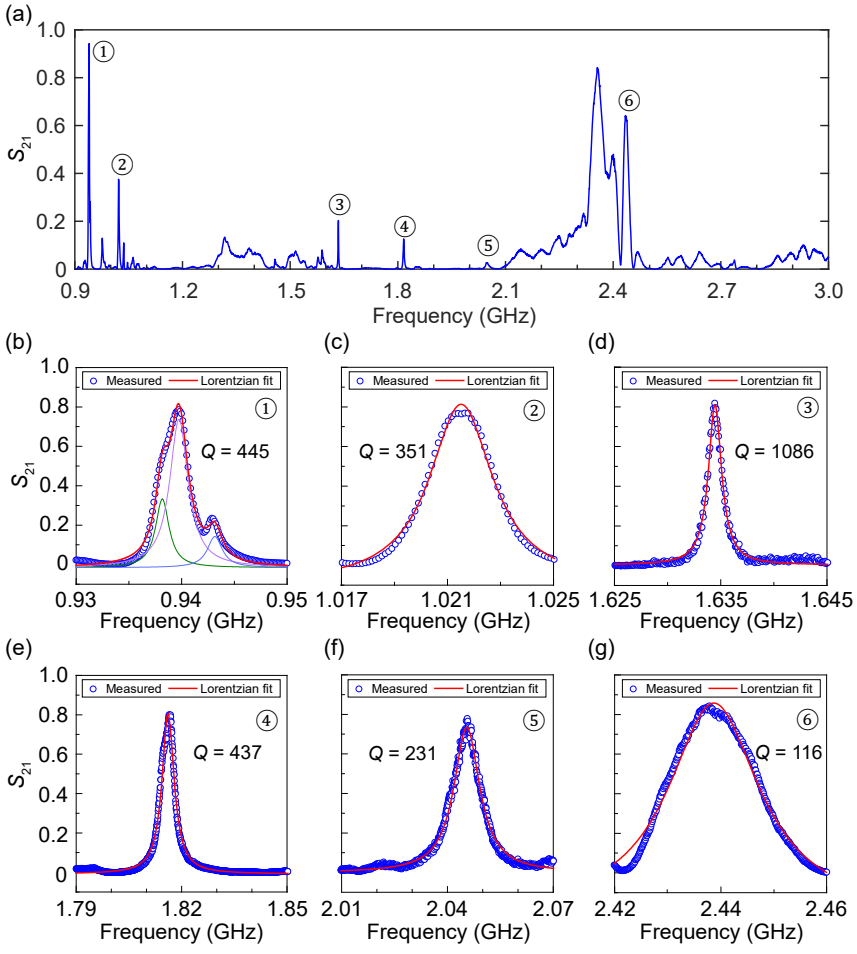

Figure 4: (a) Measured S_{21} spectrum of the fabricated device, which shows the frequency response of acousto-optic modulation. (b)–(g) Individual zoomed-in spectra for the SAW modes labeled in (a). The blue dots represent the measured data and the red lines are the corresponding Lorentzian fits.

enhanced acousto-optic modulation strength. We measured acousto-optic modulation of a racetrack microcavity with the modulation frequency up to 2.44 GHz. Our work can be extended for realizing photon–phonon coupling in the resolved-sideband regime, a prerequisite for coherent coupling between microwave and optical photons and for the associated phenomena such as electro-acousto-optically induced transparency and absorption [26]. Our devices demonstrating the application of BICs in the near-visible wavelength range will pave the way for BIC-based visible integrated photonic circuitry. These devices will also enable on-chip acousto-optic applications at visible wavelengths, such as optical filtering, microwave signal processing, and nonreciprocal light transmission.

4 Experimental section

The devices were fabricated on a *z*-cut lithium-niobate-on-insulator wafer purchased from NANOLN, where the thickness of the lithium niobate layer is 150 nm. We first fabricated the SAW IDTs on the substrate with electron-beam lithography, followed by metal deposition and a lift-off process. During the metal deposition, stacked layers of titanium (5 nm thick) and gold (60 nm thick) were deposited on the wafer. After fabrication of the SAW IDTs, we patterned the photonic waveguides, microcavities, and grating couplers in a polymer (ZEP520A) with a second step of electron-beam lithography. The polymer has a thickness of 400 nm, which was produced by spin-coating at a speed of 3000 r/min.

Author contributions: All the authors have accepted responsibility for the entire content of this submitted manuscript and approved submission.
Research funding: This work was supported by the Research Grants Council of Hong Kong (Project Nos. 14208717, 14206318, 14209519, N_CUHK415/15) and the National Natural Science Foundation of China (Grant No. 51561165012).
Conflict of interest statement: The authors declare no conflicts of interest regarding this article.

References

[1] P. Muellner, E. Melnik, G. Koppitsch, J. Kraft, F. Schrank, and R. Hainberger, "CMOS-compatible Si_3N_4 waveguides for optical biosensing," *Procedia Eng.*, vol. 120, pp. 578–581, 2015.
[2] T. Claes, W. Bogaerts, and P. Bienstman, "Experimental characterization of a silicon photonic biosensor consisting of two cascaded ring resonators based on the Vernier-effect and introduction of a curve fitting method for an improved detection limit," *Opt. Express*, vol. 18, pp. 22747–22761, 2010.
[3] I. Goykhman, B. Desiatov, and U. Levy, "Ultrathin silicon nitride microring resonator for biophotonic applications at 970 nm wavelength," *Appl. Phys. Lett.*, vol. 97, p. 081108, 2010.
[4] A. I. Lvovsky, B. C. Sanders, and W. Tittel, "Optical quantum memory," *Nat. Photonics*, vol. 3, pp. 706–714, 2009.
[5] K. F. Reim, P. Michelberger, K. C. Lee, J. Nunn, N. K. Langford, and I. A. Walmsley, "Single-photon-level quantum memory at room temperature," *Phys. Rev. Lett.*, vol. 107, p. 053603, 2011.
[6] O. Katz and O. Firstenberg, "Light storage for one second in room-temperature alkali vapor," *Nat. Commun.*, vol. 9, p. 2074, 2018.
[7] D. F. Phillips, A. Fleischhauer, A. Mair, R. L. Walsworth, and M. D. Lukin, "Storage of light in atomic vapor," *Phys. Rev. Lett.*, vol. 86, pp. 783–786, 2001.
[8] T. Udem, R. Holzwarth, and T. W. Hänsch, "Optical frequency metrology," *Nature*, vol. 416, pp. 233–237, 2002.
[9] J. Kitching, E. A. Donley, S. Knappe, et al., "NIST on a chip: realizing SI units with microfabricated alkali vapour cells," *J. Phys. Conf. Ser.*, vol. 723, p. 012056, 2016.
[10] S. Romero-García, F. Merget, F. Zhong, H. Finkelstein, and J. Witzens, "Silicon nitride CMOS-compatible platform for integrated photonics applications at visible wavelengths," *Opt. Express*, vol. 21, pp. 14036–14046, 2013.
[11] E. S. Hosseini, S. Yegnanarayanan, A. H. Atabaki, M. Soltani, and A. Adibi, "High quality planar silicon nitride microdisk resonators for integrated photonics in the visible wavelength range," *Opt. Express*, vol. 17, pp. 14543–14551, 2009.
[12] M. Khan, T. Babinec, M. W. McCutcheon, P. Deotare, and M. Lončar, "Fabrication and characterization of high-quality-factor silicon nitride nanobeam cavities," *Opt. Lett.*, vol. 36, pp. 421–423, 2011.
[13] D. J. Moss, R. Morandotti, A. L. Gaeta, and M. Lipson, "New CMOS-compatible platforms based on silicon nitride and Hydex for nonlinear optics," *Nat. Photonics*, vol. 7, pp. 597–607, 2013.
[14] Y. Gong and J. Vučković, "Photonic crystal cavities in silicon dioxide," *Appl. Phys. Lett.*, vol. 96, p. 031107, 2010.
[15] S. H. Lee, D. Y. Oh, Q.-F. Yang, et al., "Towards visible soliton microcomb generation," *Nat. Commun.*, vol. 8, p. 1295, 2017.
[16] C. Xiong, W. H. Pernice, X. Sun, C. Schuck, K. Y. Fong, and H. X. Tang, "Aluminum nitride as a new material for chip-scale optomechanics and nonlinear optics," *New J. Phys.*, vol. 14, p. 095014, 2012.
[17] P. P. J. Schrinner, J. Olthaus, D. E. Reiter, and C. Schuck, "Integration of diamond-based quantum emitters with nanophotonic circuits," *Nano Lett.*, vol. 20, pp. 8170–8177, 2020.
[18] B. Desiatov, A. Shams-Ansari, M. Zhang, C. Wang, and M. Lončar, "Ultra-low-loss integrated visible photonics using thin-film lithium niobate," *Optica*, vol. 6, pp. 380–384, 2019.
[19] R. S. Weis and T. K. Gaylord, "Lithium niobate: summary of physical properties and crystal structure," *Appl. Phys. A*, vol. 37, pp. 191–203, 1985.
[20] C.-L. Zou, J.-M. Cui, F.-W. Sun, et al., "Guiding light through optical bound states in the continuum for ultrahigh-Q microresonators," *Laser Photonics Rev.*, vol. 9, pp. 114–119, 2015.

[21] Z. Yu, X. Xi, J. Ma, H. K. Tsang, C.-L. Zou, and X. Sun, "Photonic integrated circuits with bound states in the continuum," *Optica*, vol. 6, pp. 1342–1348, 2019.
[22] S.-T. Peng, and A. A. Oliner, "Guidance and leakage properties of a class of open dielectric waveguides: part I – mathematical formulations," *IEEE Trans. Microw. Theor. Tech.*, vol. 29, pp. 843–855, 1981.
[23] K. Ogusu, "Optical strip waveguide: a detailed analysis including leaky modes," *J. Opt. Soc. Am.*, vol. 73, pp. 353–357, 1983.
[24] M. A. Webster, R. M. Pafchek, A. Mitchell, and T. L. Koch, "Width dependence of inherent TM-mode lateral leakage loss in silicon-on-insulator ridge waveguides," *IEEE Photonics Technol. Lett.*, vol. 19, pp. 429–431, 2007.
[25] Z. Yu, Y. Tong, H. K. Tsang, and X. Sun, "High-dimensional communication on etchless lithium niobate platform with photonic bound states in the continuum," *Nat. Commun.*, vol. 11, p. 2602, 2020.
[26] Z. Yu and X. Sun, "Acousto-optic modulation of photonic bound state in the continuum," *Light Sci. Appl.*, vol. 9, p. 1, 2020.
[27] Y. Wang, Z. Yu, Z. Zhang, et al., "Bound-states-in-continuum hybrid integration of 2D platinum diselenide on silicon nitride for high-speed photodetectors," *ACS Photonics*, vol. 7, pp. 2643–2649, 2020.
[28] Z. Yu, Y. Wang, B. Sun, et al., "Hybrid 2D-material photonics with bound states in the continuum," *Adv. Opt. Mater.*, vol. 7, p. 1901306, 2019.
[29] M. Mahmoud, A. Mahmoud, L. Cai, et al., "Novel on chip rotation detection based on the acousto-optic effect in surface acoustic wave gyroscopes," *Opt. Express*, vol. 26, pp. 25060–25075, 2018.
[30] Z. Yu and X. Sun, "Gigahertz acousto-optic modulation and frequency shifting on etchless lithium niobate integrated platform," *ACS Photonics*, vol. 8, pp. 798–803, 2021.
[31] L. Shao, N. Sinclair, J. Leatham, et al., "Integrated microwave acousto-optic frequency shifter on thin-film lithium niobate," *Opt. Express*, vol. 28, pp. 23728–23738, 2020.
[32] E. A. Kittlaus, W. M. Jones, P. T. Rakich, N. T. Otterstrom, R. E. Muller, and M. Rais-Zadeh, "Electrically driven acousto-optics and broadband non-reciprocity in silicon photonics," *Nat. Photonics*, vol. 15, pp. 43–52, 2021.
[33] A. E. Hassanien, S. Link, Y. Yang, E. Chow, L. L. Goddard, and S. Gong, "Efficient and wideband acousto-optic modulation on thin-film lithium niobate for microwave-to-photonic conversion," *Photonics Res.*, vol. 9, pp. 1182–1190, 2021.
[34] M. Katzman, D. Munk, M. Priel, et al., "Surface acoustic microwave photonic filters in standard silicon-on-insulator," *Optica*, vol. 8, pp. 697–707, 2021.
[35] J. Xu and R. Stroud, *Acousto-Optic Devices: Principles, Design, and Applications*, New York, USA, Wiley, 1992.
[36] M. Moharam and L. Young, "Criterion for Bragg and Raman-Nath diffraction regimes," *Appl. Opt.*, vol. 17, pp. 1757–1759, 1978.